Testing and analysis of optimised wire arc additively manufactured steel trusses

Kyvelou, P.[1], Spinasa, A.[2] and Gardner, L.[3]

[1] Imperial College London, South Kensington Campus, SW7 2AZ, London, UK
pinelopi.kyvelou@imperial.ac.uk (corresponding author)
[2] Imperial College London, South Kensington Campus, SW7 2AZ, London, UK
a.spinasa22@imperial.ac.uk
[3] Imperial College London, South Kensington Campus, SW7 2AZ, London, UK
leroy.gardner@imperial.ac.uk

ABSTRACT

Wire arc additive manufacturing (WAAM) is a method of metal 3D printing that can be used to fabricate large-scale elements of complex form, opening up opportunities to unleash the full potential of structural optimisation. To demonstrate this potential, optimised steel trusses have been fabricated by means of WAAM and tested to investigate their structural performance. The tested metal 3D printed specimens, which are considered to be the first optimised WAAM structural systems of this kind and scale, comprised members of tubular cross-section with varying diameters and thicknesses. Three different configurations were considered: cantilever, propped cantilever and simply supported, all 2 m in length. Repeat tests enabled the variability in response between specimens to be evaluated; 6 optimised trusses were tested in total. The geometric features of the tested specimens were determined using 3D laser scanning, while digital image correlation was employed to monitor the displacement and strain fields during testing. Full details of the experimental programme are provided; the obtained results are analysed and comparisons against equivalent conventional reference designs are made. The results of complementary numerical simulations, undertaken to gain further insight into particular features of the structural response of the examined specimens, are also presented. The structural efficiency of the optimised trusses, as measured by the capacity-to-mass ratio, was found to be up to 95% higher than that of the corresponding reference designs, underlining the benefits in terms of structural efficiency that can be achieved by the combination of WAAM with optimisation methods.

Keywords: digital image correlation, finite element modelling, optimised trusses, physical tests, structural efficiency, wire arc additive manufacturing

1. INTRODUCTION

Over the past few years, metal additive manufacturing (AM) has been gaining traction in a number of industries and disciplines, including the aeronautical, automotive, bioengineering and maritime sectors (Ni *et al*., 2019; Tas and Sener, 2019; Vasco, 2021; Yusuf *et al*., 2019). Recent advances, including the introduction of wire arc additive manufacturing (WAAM), a directed energy deposition (DED) AM method, now offer the potential to bring greater automation, increased build speeds, enhanced geometric freedom, relatively low manufacturing costs and practically unlimited build sizes to the construction sector (Camacho *et al*., 2018; Evans *et al*., 2022; Gardner, 2023; Guo *et al*., 2022; Kanyilmaz *et al*., 2022; Paolini *et al*., 2019).

Structural optimisation is a powerful tool with the potential to enable more sustainable and more efficient structures. In the area of steel structures, optimisation techniques have been adopted to generate optimised geometries for both conventionally manufactured (Hamidavi *et al*., 2020; Gatheeshgar *et al*., 2020; Mojtabaei *et al*., 2021; Phan *et al*., 2019) and 3D printed (Plocher and Panesar, 2019; Ribeiro *et al*., 2021) structural elements. Having few geometric restrictions, WAAM constitutes the ideal technique for the implementation of optimisation solutions, allowing the manufacture of material efficient structures of intricate shapes. Several steps have already been made towards this direction, with advanced optimisation methods being adopted to design novel AM connections (Galjaard *et al*., 2015; MX3D, 2023; Lange *et al*., 2020) and to achieve optimal performance for AM structural elements at the material (Bruggi *et al*., 2021; Li *et al*., 2020), cross-sectional (Meng *et al*., 2023; Pan *et al*., 2023; Wang *et al*., 2021; Zhang *et al*., 2022) and member levels (Laghi *et al*., 2020).

Seeking to illustrate the benefits that can be gained in terms of structural efficiency and automation by the combination of optimisation methods and AM, an end-to-end framework for the design, optimisation and fabrication of generic WAAM trusses has been proposed by Ye *et al*. (2021). Based on this framework, 2 m long WAAM trusses with three different boundary configurations and comprising members of tubular cross-section of varying diameter and thickness were produced. A summary of the optimisation and fabrication process of these trusses is presented in Section 2 of this paper. To demonstrate their structural efficiency, an experimental investigation featuring material tests,

detailed geometric measurements and in-plane bending tests on the trusses was undertaken. Full details of the experimental programme are presented in Section 3, along with an extensive analysis of the test results. Finally, in Section 4, the structural performance of the trusses is compared against complementary numerical simulations, as well as against reference designs featuring conventional hot-rolled steel sections.

2. OPTIMISATION AND MANUFACTURING OF SPECIMENS

An end-to-end framework for the design, optimisation and manufacture of generic tubular trusses has been established by Ye *et al*. (2021). Based on this framework, three different types of trusses were generated, each corresponding to a different boundary configuration: cantilever, propped cantilever and simply supported. The examined load cases featured typical load levels met in residential buildings. Layout optimisation and geometry rationalisation were first employed to determine the topology of the trusses, accounting for all manufacturing and practical constraints. Cross-section optimisation was then undertaken, resulting in members of tubular cross-section of varying diameter and thickness. Finally, a series of geometric operations was undertaken for the automatic determination of the geometry of the joints connecting the optimised tubular truss members.

Following determination of the final optimised geometries, the optimal printing sequences were established. For each truss, recurring geometric features that could be manufactured using the same printing strategy were first identified and then grouped into broader zones of similar build sequence. The printing layer orientation for each truss segment was then determined, aiming to maintain vertical printing as far as possible, while minimising the substrate orientation. More details regarding the process followed to ensure printability of the optimised trusses have been provided by Ye *et al*. (2021).

All trusses were manufactured by the Dutch company MX3D (2022), using ER70S-6 (EN ISO 14341-A G 42 3 M21 3Si1) feedstock wire of 1.2 mm diameter. The mechanical properties of the as-welded wire, as provided by the manufacturer, are reported in Table 1. A 6-axis ABB robot, integrated with a metal inert gas (MIG) welding system and equipped with a moving substrate, was employed for the fabrication of the WAAM specimens. The employed shielding gas was 80% Ar + 20% CO_2, while the adopted welding method was short-arc. A summary of the process parameters utilised during printing

is presented in Table 2. The optimised trusses, shown in Figure 1, featured members of two different nominal thicknesses (i.e. t_{nom} = 3.5 mm and t_{nom} = 4.5 mm) as shown in Figure 2 and of various nominal diameters, as reported in Figure 3. Close-up views of typical nodes adjoining the tubular truss members are shown in Figure 4.

Note that one repeat specimen was manufactured for each truss type (i.e. cantilever, propped cantilever and simply supported), in order to evaluate the variability in response between nominally identical specimens.

3. EXPERIMENTAL PROGRAMME

A comprehensive experimental programme was undertaken in the Structures Laboratory in the Department of Civil and Environmental Engineering at Imperial College London, featuring material tests, followed by in-plane bending tests on the optimised trusses up to failure. A detailed description of the adopted test methods and instrumentation, as well as of the obtained results, is presented in this section. Note that some preliminary results of this testing programme have been reported by Kyvelou *et al*. (2023).

3.1 Material tests

The mechanical properties of the optimised truss material were determined by means of tensile coupon tests, conducted in line with EN ISO 6892-1 (2016). Dog-bone shaped coupons were extracted from WAAM flat plates, which were manufactured using the same printing parameters and feedstock wire as used for the trusses. The influence of the coupon thickness and WAAM surface undulations on the mechanical properties of the WAAM material was examined by testing coupons of two different nominal thicknesses (i.e. 3.5 mm and 8.0 mm) and surface finishes (i.e. as-built undulating and machined flat), while the material anisotropy was investigated by testing coupons extracted at different angles to the print layer orientation. The dimensions of the tested coupons, shown in Figure 5(a), were determined according to EN ISO 6892-1 (2016), while the employed test setup is presented in Figure 5(b). The tensile load was applied by a 250 kN Instron 8800 testing machine using displacement control, while a four-camera LaVision digital image correlation (DIC) system was employed to monitor the

evolution of the strain fields on both coupon sides during testing. A detailed description of the conducted tests and an extensive analysis of the obtained results has been provided by Huang *et al*. (2022).

Mild material anisotropy was observed, while the influence of both the coupon thickness and surface undulations on the obtained material response was found to be slightly more pronounced. Thus, the material response of the trusses was assumed to be isotropic, but to vary with thickness. The adopted mechanical properties were assumed to be equal to the effective material properties of the as-built coupons (i.e. where the surface undulations were not removed), tested at 90° to the print layer orientation, mirroring the condition of the trusses, as given in Table 3, where E is the Young's modulus, v is the Poisson's ratio, f_y and f_u are the yield and ultimate tensile strengths respectively and ε_u is the strain at f_u. The mechanical properties obtained from the as-built coupons are referred to as 'effective' since their values are affected by the surface undulations. Note that the mechanical properties for the 4.5 mm thick elements were determined by means of linear interpolation between the properties determined for the 3.5 mm and 8.0 mm thick coupons reported by Huang *et al*. (2022), since it has been shown that the material properties of WAAM elements reduce with increasing thickness due to the longer cooling times (Huang *et al*., 2022). However, as can be seen from Table 3, the difference in mechanical propertied between the 3.5 mm and 8.0 mm material is relatively small, suggesting that the impact of the linear interpolation assumption is also small.

3.2 Geometric measurements

3D laser scanning was employed to obtain the geometry of the WAAM trusses digitally, since their undulating as-built surface and intricate geometry, shown in Figure 4, rendered conventional calliper measurements impractical. A Faro ScanARM, integrated with a FARO laser line probe and providing rapid data capture of up to 600,000 points per second with a reported accuracy of 0.1 mm and a resolution of 0.075 mm, was employed for the laser scans – see Figure 6(a). The scan data of each truss were converted from a point cloud into a polygonal mesh, using the software Geomagic Wrap (2017) – see Figure 6(b) and 6(c). Subsequently, the digital models featuring the scanned geometry of the trusses were compared against the respective digital models with the nominal geometries, to detect the magnitude and distribution of the geometric deviations. The generated geometric deviation maps of all

trusses are shown in Figure 7, where differences up to about 3.5 mm can be observed between the scanned and nominal geometry of the truss members.

For each truss, the 3D model of each tubular member was isolated and imported into Rhino 3D (2017) as an STL file for its geometric characteristics to be obtained. Each member was first reoriented using principal component analysis (Hotelling, 1933; Pearson, 1901), such that its longitudinal axis aligned with the global x-axis – see Figure 8. Following alignment, each member was contoured at 0.1 mm intervals along its longitudinal axis (Huang *et al.*, 2022). The outer diameter D, thickness t and eccentricities between the centroid of each cross-section cut i and the overall centroid of the member along the y and z axes (labelled as $e_{y,i}$ and $e_{z,i}$ respectively) were subsequently determined, following the process described by Weber *et al*. (2023) – see Figure 8. It should be mentioned that the thickness of each truss member was determined after completion of the physical experiments, by slicing and scanning the tubular members that had experienced the lowest stress levels during testing (identified through the digital image correlation (DIC) data – see Section 3.3.3).

The adopted labelling system starts with the letters C, PC or SS for the cantilever, propped cantilever or simply supported trusses respectively, followed by the test number. Comparisons between the nominal and average measured geometric properties of all trusses are presented in Figure 9 and Table 4, where D_{nom}, t_{nom} and A_{nom} are the nominal outer diameter, thickness and cross-sectional area of the tubular truss members respectively, while D_{scan}, t_{scan} and A_{scan} are the average measured (by means of laser scanning) outer diameter, thickness and cross-sectional area of the tubular truss members respectively. A comparison between the measured and nominal masses of the trusses (labelled as m_m and m_{nom} respectively) is also reported. Finally, the amplitude of the geometric imperfections of each tubular truss member e was determined as the maximum of the Euclidean norms of the eccentricities e_y and e_z for each cross-section cut i, labelled e_i – see Figure 10, while, for each truss, the member imperfection amplitude e_{imp}, reported in Table 4, was defined as the maximum value of e of all truss members.

The scanned diameters D_{scan} were found to be consistently lower than the nominal diameters D_{nom} for all trusses (by 4% on average), while the scanned thicknesses t_{scan} were generally greater than the nominal thicknesses t_{nom}. Overall, the measured masses m_m of the trusses and the cross-sectional areas

A_{scan} of their members were similar to the nominal values (m_{nom} and A_{nom} respectively), with the exception of specimen C1, whose measured mass and average cross-sectional area were found to be 18% lower than the respective nominal values. The below-target mass of Specimen C1 is related to the fact that this specimen was the first optimised truss to be printed and served, to some extent, as a "testing ground" for the remainder of the trusses. Therefore, during the production cycle of this specimen, several process parameters were being fine-tuned, resulting in a slightly less homogeneous print and, eventually, in the overall mass and cross-section proportions being somewhat below the target. The measured imperfection amplitudes e_{imp} of the truss members were generally found to lie between about 1.3 mm and 1.8 mm, while the average value of the imperfection amplitudes of all truss members was found to be equal to $L/325$, where L is the member length; this imperfection amplitude is greater than the value of $L/1000$ assumed in the development of Eurocode 3 for the design of conventionally manufactured structural steel members (Beer and Schulz, 1970; Meng and Gardner, 2020), and is indicative of the fact that WAAM elements are generally likely to have higher geometric imperfections relative to equivalent rolled steel members.

3.3 Test setup and instrumentation

Following completion of the geometric measurements, the optimised trusses were tested to failure for their structural response to be assessed. The experimental setup, as well as the employed instrumentation, are described in this section.

3.3.1 Test rig and loading scheme

The setup used for the conducted truss experiments is illustrated in Figure 11. The purpose-built test rig, which was designed to be adjustable to the three different boundary configurations of the examined specimens (i.e. cantilever, propped cantilever and simply supported), consisted of a support frame, a top loading beam, a shear wall, a hydraulic actuator and a lateral restraint system. The load was applied by a 500 kN Instron hydraulic actuator mounted on the loading beam, using displacement control at a constant rate of 0.5 mm/min.

The fixed end boundary conditions (used for the cantilever and propped cantilever trusses) were achieved by fixing two load transfer plates, with one pin on each one of them, to the shear wall – see

Figure 12(a), while for the simply supported truss, only one of the two pins was used to provide the pinned support at one end – see Figure 12(b). For the other end of the propped cantilever and simply supported trusses, a roller moving on steel rails was employed, allowing for the axial displacement of the truss – see Figure 12(c). The cantilevers were loaded at their tip through a flat plate, while for the rest of the trusses, which were loaded at midspan, a steel saddle of the same curvature as the truss top chord at midspan was manufactured and mounted on the truss – see Figure 12(d). Note that adhesive was used to fill any gaps between the saddle and the top chord of the truss, to ensure uniform load application.

3.3.2 Lateral restraint system

To ensure in-plane bending, a bespoke lateral restraint system was employed, designed to prevent out-of-plane instability of the test specimens without inducing any undesirable in-plane restraint. Triangular-shaped plated elements were printed directly on both sides of the compressive chord of the trusses (i.e. bottom chord for the cantilevers and top chord for the propped cantilever and simply supported trusses), where threaded steel bars were connected by means of bolts – see Figure 13(a). As shown in Figure 13(b), these bars were mounted on sliders at the restrained end, which followed the vertical in-plane deflection of the specimens, while load cells were employed to monitor the restraint forces that developed during testing at each restraint position. Any lateral deflections observed during testing were removed by manually loosening or tightening the respective threaded bars with ratchet spanners, pulling the specimen back to straightness – see Figure 13(c), though minimal adjustment was required. An overview of the lateral restraint system is presented in Figures 13(d) and 13(e), for typical trusses restrained at their bottom and top chord, respectively.

3.3.3 Instrumentation

All trusses were extensively instrumented, as shown in Figure 14, using both conventional and non-contact measurement instrumentation. Five string potentiometers (SP), affixed to the bottom chord of the trusses at the locations of the lateral restraints, were employed to measure the vertical deflections during testing. A linear variable displacement transducer (LVDT), monitoring vertical deflections, was also used at the point of load application (i.e. cantilever tip for the cantilevers and midspan for the

propped cantilever and simply supported trusses). Finally, measurements of the deflections occurring due to deformations of the test rig were also taken. The vertical deflections occurring due to support sinking were measured by vertical LVDTs located underneath the supports, while the horizontal deflections of the shear wall at the fixed end was measured by means of a pair of LVDTs, positioned horizontally at the locations of the two pins – see Figure 14. All test outputs, namely the load applied by the hydraulic actuator, the vertical displacements measured by the SPs and the LVDTs, the horizontal and vertical deflections measured at the supports and the restraint forces, were continuously monitored and recorded at a frequency of 1Hz, using the data acquisition system DATASCAN.

In addition to the conventional instrumentation described above, non-contact digital image correlation (DIC) was also employed to enable full-field measurements of displacements and strains to be captured. The DIC setup is shown in Figure 15. A four-camera LaVision DIC system was utilised for image acquisition, capturing images at a rate of 0.5 Hz, which were processed using the software package DaVis 10 (LaVision, 2017). Prior to testing, the side of the specimen that would be monitored by the DIC cameras was wire-brushed to remove any welding soot arising from the WAAM process, and was then sprayed with a thin layer of matt black paint, to eliminate reflection during image acquisition. Finally, a random white speckle pattern was applied on the monitored surface, with an average speckle size of three to five pixels in the acquired DIC images. The steps followed in preparing the surfaces for DIC image acquisition are illustrated in Figure 16.

3.4 Test results

The failure modes of the trusses are shown in Figure 17. All test specimens failed by tensile fracture of a 3.5 mm thick tubular member, with the exception of Specimen SS1, which failed by buckling of a 3.5 mm thick tubular member within the top chord – see Figure 17(e). A typical DIC strain field at the peak load is presented in Figure 18(a) for Specimen C1, where all truss members may be seen to be heavily stressed, reflecting the full material usage achieved due to the optimised geometry. In Figure 18(b), a close-up view of the strain field at the location of fracture is shown, where the strain levels can be observed to be close to the ultimate tensile strain of the material (i.e. $\varepsilon_u = 0.13$).

The load-deflection curves of all specimens are presented in Figure 19, where the total vertical load P is plotted against the vertical deflection at the cantilever tip δ_{tip} for the cantilevers, and against the midspan vertical deflection δ_{mid} for the propped cantilever and simply supported trusses. The ultimate load of Specimen C1 was 22% lower than that of Specimen C2, with this discrepancy being attributed primarily to the mass and cross-sectional areas of the former being 18% lower than that of the latter (see Table 4), as discussed in Section 3.2.

The propped cantilever specimens reached similar peak loads, with less than 2% difference between them. Note that the drops in the load-deflection curve of Specimen PC1 were caused by some slippage of the top pin at the fixed end during testing. Finally, although the masses of the simply supported specimens were similar (m_{SS1}/m_{SS2} = 1.01), the ultimate load of Specimen SS2 was 30% lower than that of Specimen SS1. Visual inspection of the cross-section of the fractured member of Specimen SS2 revealed substantial porosity, which was measured to be equal to 45% of the scanned cross-sectional area A_{scan}, following the process described by Chong *et al*. (2021) – see Figure 20(a). Examination of the printing logs at the general area of fracture did not reveal any variation in the process parameters employed – see Figure 20(b). However, as shown in Figure 20(c), at the specific fracture location, some monitoring data were missing, indicating that the logging system was not recording. This signifies that the system was operating in manual (rather than automatic) mode, which is common practice following a pause (e.g. overnight) in printing. Following an extended investigation by the manufacturers, it was concluded that the porosity observed at the fracture location most likely occurred due to human error while the system was operating in manual mode, resulting in an unintended lack of shielding gas. This incident emphasises the need for continuous logging of the process parameters during printing as part of the quality control procedure for 3D printed structural components.

4. EVALUATION OF STRUCTURAL RESPONSE

The structural response and efficiency of the optimised trusses are evaluated in this section, by means of comparisons against complementary finite element (FE) models, as well as against reference designs featuring hot-rolled steel I-sections.

4.1 Comparisons against numerical simulations

Complementary finite element (FE) modelling of the optimised trusses was undertaken in parallel with the experimental programme. The FE models, which are shown in Figure 21, were developed using the FE package ABAQUS (2021) and were used to gain further insight into the structural response and load-bearing capacity of the tested trusses.

The development of the FE simulations was initiated by importing the nominal geometry of the trusses into ABAQUS (2021) from a 3D CAD model created in Rhino 3D (2017), which was also used for the printing of the trusses. Corresponding FE models based on the measured geometry of the trusses were also created, by adjusting the thickness of the truss members to match the respective cross-sectional areas as determined by laser scanning. General purpose 4-noded quadrilateral S4R shell elements with reduced integration and hourglass control (ABAQUS, 2021) were employed for discretising the truss models; this element type has been successfully employed in similar previous applications (Theofanous *et al*., 2009; Zhao *et al*., 2016). The stress-strain response of the WAAM material was taken into account through the constitutive model established by Huang *et al*. (2023), in combination with the key mechanical properties reported in Table 5. The resulting stress-strain curves were incorporated into ABAQUS (2021) in multi-linear form, as described by a series of true stress – true plastic strain data points. Initial geometric imperfections were taken into consideration by means of the first positive eigenmode determined by means of a linear buckling analysis, amplified by the measured imperfection values e_{imp} reported in Table 6.

Comparisons between the test and FE load-deformation curves (both for the nominal and measured specimen geometries, denoted as FE_{nom} and FE_{meas} respectively) are illustrated in Figure 22, where the total vertical load P is plotted against the average normalised axial deformation of the top chord of the trusses $\Delta L/L$. Note that the value of the axial deformation ΔL of the top chord of the trusses was determined at each load increment i, in line with Equation (1), as the difference between the length of the top chord L_i and its initial value prior to loading L_0 – see Figure 23, where the parameters used in Equation (1) are defined. As shown in Figure 22, the FE models were found to yield fairly accurate predictions of the general load-deformation response, especially when the measured geometries were

297 employed. Note however that fracture is not explicitly considered in the current FE simulations,
298 meaning that the abrupt failures observed in some of the tests (PC1, PC2 and SS2) were not well
299 captured.

$$\Delta L = L_i - L_0 = \sqrt{\left(L_0 + \delta_{x,2} - \delta_{x,1}\right)^2 + \left(\delta_{y,2} - \delta_{y,1}\right)^2 + \left(\delta_{z,2} - \delta_{z,1}\right)^2} - L_0 \quad (1)$$

300
301 In Table 5, the ratios of the ultimate loads attained by the test specimens $P_{u,test}$ to those predicted by the
302 FE models with the nominal and measured truss geometries ($P_{u,FEnom}$ and $P_{u,FEmeas}$ respectively) are
303 presented. The test capacity of Specimen C1 can be seen to be 26% lower that its corresponding nominal
304 value (i.e. as predicted by the FE model with the nominal geometry); this is attributed to the deviation
305 between the nominal and measured geometry (see Table 4) since, when the latter is taken into
306 consideration (through the use of the FE model with the measured geometry), its capacity is accurately
307 predicted. The largest deviation between the test results and the FE predictions was observed for
308 Specimen SS2, with the ultimate load measured during the test being 35% lower than predicted; this is
309 attributed to the high porosity observed for this specimen (see Section 3.4), which was not considered
310 in the FE model and highlights the need for further improvements in monitoring and quality control to
311 support the wider application of this manufacturing technology (Gardner, 2023). For the remainder of
312 the test specimens, the FE predicted capacities were reasonably accurate, being within 10% on average
313 of the experimental results.
314 A tentative gauging of structural reliability is now presented, in which first characteristic (5 percentile)
315 resistances and then, through the application of a suitable partial safety factor, design (0.1 percentile)
316 resistances for the trusses are sought. The FE models were employed for the determination of the
317 characteristic resistances of the optimised trusses. The characteristic values of the material properties
318 were determined based on a dataset comprising tensile test results from 67 WAAM coupons (Guo *et*
319 *al*., 2022; Huang *et al*., 2022; Kotteman, 2020; Michl *et al*., 2020; Müller *et al*., 2019; Silvestru *et al*.,
320 2021; Tankova *et al*., 2022) loaded at 90° to their print layer orientation and manufactured using ER70S-
321 6 feedstock wire, mirroring the condition of the truss members. A normal distribution was fitted to the
322 histogram of the mechanical properties of the examined dataset, and the characteristic values were
323 determined based on a non-exceedance probability of 5%, in line with Annex E of prEN 1993-1-1

(2020). The characteristic values of the Young's modulus E_k, yield strength $f_{y,k}$ and ultimate strength $f_{u,k}$ were determined to be 170000 MPa, 260 MPa and 380 MPa respectively; hence, these values were used in the numerical simulations in conjunction with the nominal geometry of the trusses, to determine the characteristic truss resistances $P_{u,k}$. The design resistances of all trusses $P_{u,d}$ were then calculated based on the characteristic resistances $P_{u,k}$, reduced by a partial safety factor γ_{M2} = 1.25. The value of γ_{M2} = 1.25 was selected based on the ratio of the 0.1 to 5 percentile yield strength from the collected WAAM material data and on its current application to welded connections (that clearly share common features with the studied WAAM structures) in EN 1993-1-8 (2005). In Figure 24, the load-deflection curves of the tested trusses are plotted, along with their corresponding characteristic and design resistances, where all trusses can be seen to exceed their design resistance $P_{u,d}$.

4.2 Comparisons against reference designs

The structural efficiency of the optimised trusses was assessed by comparing their performance, evaluated by the capacity-to-mass ratio, against equivalent reference designs. Conventional beams were designed for the examined load case scenarios, with standard hot-rolled S355 UB sections selected. Comparisons between the optimised trusses and their corresponding reference designs (denoted by 'ref') are presented in Table 5. The capacity-to-mass ratio of the optimised trusses was, in all cases, higher than the equivalent ratio of the corresponding reference UB sections, confirming the efficiency of the examined optimised designs. With the exception of Specimen SS2, which exhibited high levels of porosity – see Section 3.4, the structural efficiency of the optimised trusses was at least 60%, and up to 95%, higher than that of the corresponding reference designs, showing that the combination of WAAM with optimisation methods can lead to the manufacture of structures with reduced material usage and improved structural performance.

5. CONCLUSIONS

An experimental investigation into the structural response of optimised WAAM trusses has been presented. The tested trusses comprised members of tubular cross-section of varying diameter and thickness. Advanced non-contact measurement techniques, featuring 3D laser scanning and digital

image correlation, were employed to determine the specimen geometry and monitor the displacement and strain fields during testing. Complementary finite element models were also developed, to help gain further insight into particular features of the structural response of the examined specimens. The key findings are listed below:

- Deviations in geometry and print quality between nominally identical truss specimens were observed, subsequently leading to commensurate differences in ultimate capacity. The necessity for quality control and constant monitoring of the process parameters during printing has been highlighted.
- The developed numerical models were found to be capable of generally capturing the structural response of the optimised WAAM trusses when accounting for the material and geometric properties of the WAAM elements.
- Utilising statistics from existing WAAM material test data, tentative characteristic mechanical properties were determined and utilised in the developed FE models to provide characteristic resistances of the examined trusses. A partial safety factor $\gamma_{M2} = 1.25$ was then applied to attain the corresponding design resistances; all tested trusses were found to exceed their design resistance.
- The structural performance of the examined trusses was evaluated by comparisons against equivalent reference hot-rolled steel designs. The capacity-to-mass ratio of the optimised trusses was found to be up to 95% higher than the equivalent ratio of the corresponding reference designs, reflecting the potential for reduced material usage and enhanced structural efficiency that can be achieved by the combination of WAAM and optimisation methods.

DATA AVAILABILITY STATEMENT

Some or all data, models, or code that support the findings of this study are available from the corresponding author upon reasonable request.

ACKNOWLEDGEMENTS

This research was possible thanks to funding and support from the European Union's Horizon 2020 research and innovation programme under grant agreement No. 820776 'Intelligent data-driven pipeline for the manufacturing of certified metal parts through Direct Energy Deposition process (INTEGRADDE).' The authors also gratefully acknowledge funding and support from the Onassis Foundation. Finally, the authors would like to thank Gordon Herbert, Zuzanna Rydz, Les Clark, Paul Crudge and Freddy Olivo for their contributions to the experimental study.

REFERENCES

ABAQUS (2021) CAE 2021, Dassault Systèmes Simulia Corp.

Beer, H. and Schulz, G. (1970) Bases théoriques des courbes européennes de flambement. *Construction Métallique*, 3, 37-57.

Bruggi, M., Laghi, V. and Trombetti, T. (2021) Simultaneous design of the topology and the build orientation of wire-and-arc additively manufactured structural elements. *Computers & Structures*, 242, 106370.

Camacho, D.D., Clayton, P., O'Brien, W.J., Seepersad, C., Juenger, M., Ferron, R. and Salamone, S. (2018) Applications of additive manufacturing in the construction industry – A forward-looking review. *Automation in Construction*, 89, 110-119.

Chong, B. W., Othman, R., Jaya, R. P., Shu Ing, D., Li, X., Ibrahim, M. H. W., Abdullah, M. M. A. B., Sandu, A. V., Płoszaj, B., Szmidla, J. and Stachowiak, T. (2021) Image Analysis of Surface Porosity Mortar Containing Processed Spent Bleaching Earth. *Materials*, 14, 1658.

EN 1993-1-8. (2005) *Eurocode 3. Design of steel structures. Part 1-8: Design of joints*. Brussels, European Committee for Standardization.

EN ISO 6892-1. (2016) *Metallic materials - Tensile testing – Part 1: Method of test at room temperature*. Brussels, European Committee for Standardization (CEN).

Evans, S.I., Wang, J., Qin, J., He, Y., Shepherd, P. and Ding, J. (2022) A review of WAAM for steel construction – Manufacturing, material and geometric properties, design, and future directions. *Structures*, 44, 1506-1522.

Galjaard, S., Hofman, S., Perry, N. and Ren, S. (2015) Optimizing Structural Building Elements in Metal by using Additive Manufacturing. In: *Proceedings of the International Association for Shell and Spatial Structures (IASS) Symposium 2015*, 17-20 August 2015, Amsterdam, The Netherlands.

Gardner, L. (2023) Metal additive manufacturing in structural engineering – review, advances, opportunities and outlook. *Structures*, 47, 2178-2193.

Gatheeshgar, P., Poologanathan, K., Gunalan, S., Tsavdaridis, K.D., Nagaratnam, B. and Iacovidou, E. (2020) Optimised cold-formed steel beams in modular building applications. *Journal of Building Engineering*, 32, 10167.

Geomagic Wrap (2017) 3D Systems, (Version 2017.0.2:64) [Software] Incorporated and its Licensors.

Guo, X., Kyvelou, P., Ye, J., Teh, L. H. and Gardner, L. (2022) Experimental investigation of wire arc additively manufactured steel single-lap shear bolted connections. *Thin-Walled Structures*, 181, 110029.

Hamidavi, T., Abrishami, S. and Hosseini, M.R. (2020) Towards intelligent structural design of buildings: A BIM-based solution. *Journal of Building Engineering*, 32, 101685.

Huang, C., Kyvelou, P. and Gardner, L. (2023) Stress-strain curves for wire arc additively manufactured steels. *Engineering Structures*, 279, 115628.

Huang, C., Kyvelou, P., Zhang, R., Britton, T. B. and Gardner, L. (2022) Mechanical testing and microstructural analysis of wire arc additively manufactured steels. *Materials & Design*, 216, 110544.

Hotelling, H. (1933) Analysis of a complex of statistical variables into principal components. *Journal of Educational Psychology*, 24, 417-441.

Kanyilmaz, A., Demir, A. G., Chierici, M., Berto, F., Gardner, L., Kandukuri, S. Y., Kassabian, P., Kinoshita, T., Laurenti, A., Paoletti, I., du Plessis, A. and Razavi, S. M. J. (2022) Role of metal 3D

printing to increase quality and resource-efficiency in the construction sector. *Additive Manufacturing*, 50, 102541.

Kotteman, G. M. G. (2020) *Steel 3D printing for structures*. PhD thesis, TU Delft.

Kyvelou, P., Spinasa, A. and Gardner, L. (2023) Testing and analysis of optimised wire arc additively manufactured steel trusses. In: *Proceedings of the 10th Eurosteel Conference (Eurosteel 2023)*, 12-14 September 2023, Amsterdam, the Netherlands [accepted]

Laghi, V., Palermo, M., Gasparini, G. and Trombetti, T. Computational design and manufacturing of a half-scaled 3D-printed stainless steel diagrid column. *Additive Manufacturing*, 36, 101505.

Lange, J., Feucht, T. and Erven, M. (2020) 3D printing with steel – additive manufacturing for connections and structures. *Steel Construction*, 13(3), 144-153.

LaVision (2017) *DaVis* (Version 8.4.0) [Software] La Vision GmbH.

Li, S., Yuan, S., Zhu, J., Wang, C., Li, J. and Zhang, W. (2020) Additive manufacture-driven design optimisation: Building direction and structural topology. *Additive Manufacturing*, 36, 101406.

Meng, X. and Gardner, L. (2020) Behavior and design of normal and high strength steel SHS and RHS columns. *Journal of Structural Engineering, ASCE*., 146(11), 04020227.

Meng, X., Weber, B., Nitawaki, M., and Gardner, L. (2023) Optimisation and testing of wire arc additively manufactured steel stub columns. *Thin-Walled Structures*, 189, 110857.

Michl, D., Sydow, B. and Bambach, M. (2020) Ring Rolling of Pre-forms Made by Wire-arc Additive Manufacturing. *Procedia Manufacturing*, 47, 342-348.

Mojtabaei, S.M., Hajirasouliha, I. and Ye, J. (2021) Optimisation of cold-formed steel beams for best seismic performance in bolted moment connections. *Journal of Constructional Steel Research*, 181, 106621.

MX3D. [online] Available from: https://mx3d.com/services/research/integradde/ [Accessed 28 Feb. 2022]

MX3D. [online] Available from: https://mx3d.com/industries/architecture-construction/ [Accessed 17 Mar. 2023]

Müller, J., Grabowski, M., Müller, C., Hensel, J., Unglaub, J., Thiele, K., Kloft, H. and Dilger, K. (2019) Design and Parameter Identification of Wire and Arc Additively Manufactured (WAAM) Steel Bars for Use in Construction. *Metals*, 9, 725.

Ni, J., Ling, H., Zhang, S., Wang, Z., Peng, Z., Benyshek, C., Zan, R., Miri, A.K., Li, Z., Zhang, X., Lee, J., Lee, K.-J., Kim, H.-J., Tebon, P., Hoffman, T., Dokmeci, M.R., Ashammakhi, N., Li, X. and Khademhosseini, A. (2019) Three-dimensional printing of metals for biomedical applications. *Material Today Bio*, 3, 100024.

Pan, J., Wang, J., Evernden, M., Tian, Y., Chater, B. and Li, R. (2023) Experimental and numerical study of 3D printed steel plates stiffened by sinusoidal waves for enhanced stability. *Engineering Structures*, 293, 116577.

Paolini, A., Kollmannsberger, S. and Rank, E. (2019) Additive manufacturing in construction: A review on processes, applications, and digital planning methods. *Additive Manufacturing*, 30, 100894.

Pearson, K. (1901) On lines and planes of closest fit to systems of points in space. *The London, Edinburgh, and Dublin Philosophical Magazine and Journal of Science*, 2, 559-572.

Phan, D.T., Mojtabaei, S.M., Hajirasouliha, I., Ye, J. and Lim, J.B.P. (2020) Coupled element and structural level optimisation framework for cold-formed steel frames. *Journal of Constructional Steel Research*, 168, 105867.

Plocher, J. and Panesar, A. (2019) Review on design and structural optimisation in additive manufacturing: Towards next-generation lightweight structures. *Materials and Design*, 183, 108164.

prEN 1993-1-1. (2020) *Eurocode 3. Design of steel structures. Part 1-1: General rules and rules for buildings.* Brussels, European Committee for Standardization.

Rhino 3D (2017) (Version 5 SR14 64-bit) 607 [Software] Robert McNeel & Associates.

Ribeiro, T.P., Bernardo, L.F.A. and Andrade, J.M.A. (2021) Topology Optimisation in Structural Steel *Applied Sciences*, 11(5), 2112.

Silvestru, V. A., Ariza, I., Vienne, J., Michel, L., Sanchez, A. M. A., Angst, U., Rust, R., Gramazio, F., Kohler, M. and Taras, A. (2021) Performance under tensile loading of point-by-point wire and arc additively manufactured steel bars for structural components. *Materials & Design*, 205, 109740.

Tankova, T., Andrade, D., Branco, R., Zhu, C., Rodriguew, D. and da Silva, L. S. (2022) Characterization of robotized CMT-WAAM carbon steel. *Journal of Constructional Steel Research*, 199, 107624.

Tas, S.O. and Sener, B. (2019) The Use of Additive Manufacturing in Maritime Industry. *International Journal of Engineering Trends and Technology*, 67(6), 47-51.

Theofanous, M., Chan, T. M. and Gardner, L. (2009) Flexural behaviour of stainless steel oval hollow sections. *Thin-Walled Structures*, 47(6-7), 776-787.

Vasco, J.C. (2021) *Additive manufacturing for the automotive industry*. [chapter 16] In: Handbooks in Advanced Manufacturing, Additive Manufacturing, Elsevier, 505-530.

Ye, J., Kyvelou, P., Gilardi, F., Lu, H., Gilbert, M. and Gardner, L. (2021) An end-to-end framework for the additive manufacture of optimized tubular structures. *IEEE Access*, 9, 165476-165489.

Yusuf, S.M., Cutler, S. and Gao, N. (2019) Review: The Impact of Metal Additive Manufacturing on the Aerospace Industry. *Metals*, 9(12), 1286.

Wang, J., Evernden, M., Chater, B. and Pan, J. (2021) Printing imperfections – geometric patterns to improve resistances of 3D printed steel plates. In: *Proceedings of the 9th European Conference on Steel and Composite Structures (Eurosteel 2021)*, 1-3 September 2021, Sheffield, UK.

Weber, B., Meng, X., Zhang, R., Nitawaki, M., Sagawa, T. and Gardner, L. (2023) Tensile behaviour of WAAM high strength steel material and members. *Materials & Design* [submitted]

Zhang, R., Meng, X. and Gardner, L. (2022) Shape optimisation of stainless steel corrugated cylindrical shells for additive manufacturing. *Engineering Structures*, 270, 114857.

Zhao, O., Gardner, L. and Young, B. (2016) Buckling of ferritic stainless steel members under combined axial compression and bending. *Journal of Constructional Steel Research*, 117, 35-48.

501 **Table 1.** Mechanical properties of as-welded ER70S-6 feedstock wire, as provided by the
502 manufacturer

Yield strength (MPa)	Tensile strength (MPa)	Elongation (%)	Impact energy at -40°C (J)
471	580	25	73

503
504

505 **Table 2.** Printing parameters employed during the WAAM process

t_{nom} (mm)	Travel speed (mm/s)	Wire feed rate (m/min)	Voltage (V)	Current (A)	Gas flow rate (L/min)	Interpass temperature (°C)
3.5	6	3.5	14-15	55-60	18	250
4.5	6	4.5	16	85-90	18	250

506
507

508 **Table 3.** Effective mechanical properties of as-built WAAM material

t_{nom} (mm)	E (GPa)	ν	f_y (MPa)	f_u (MPa)	ε_u
3.5	201.2	0.29	345	458	0.130
4.5*	198.4	0.29	330	444	0.134
8.0	188.4	0.28	278	395	0.150

509 *Mechanical properties of 4.5 mm material were interpolated between those of tested 3.5 mm and 8.0
510 mm material. The latter are reported for information only.
511

512 **Table 4.** Comparisons between nominal and average measured geometric properties

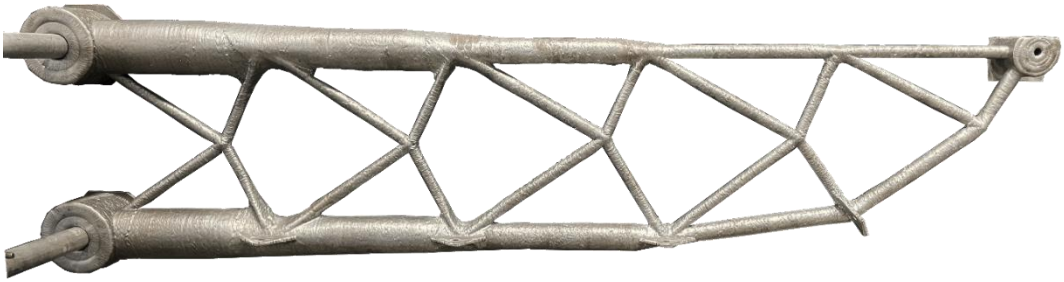
Truss type	Specimen ID	D_{scan}/D_{nom}	t_{scan}/t_{nom} (t_{nom}=3.5 mm)	t_{scan}/t_{nom} (t_{nom} = 4.5 mm)	A_{scan}/A_{nom}	m_m/m_{nom}	e_{imp} (mm)
Cantilever	C1	0.95	0.91	0.78	0.82	0.82	1.28
	C2	0.96	1.05	0.96	0.97	1.00	1.84
Propped cantilever	PC1	0.95	1.06	1.09	0.99	0.98	1.54
	PC2	0.96	1.05	1.08	0.99	0.98	1.59
Simply supported	SS1	0.96	1.07	0.98	1.01	1.00	1.50
	SS2	0.96	1.04	0.98	0.99	0.99	1.42

513
514

515 **Table 5.** Performance assessment of WAAM trusses

Truss type	Specimen	$P_{u,test}/P_{u,FEnom}$	$P_{u,test}/P_{u,FEact}$	$\frac{P_{u,test}/m_w}{P_{u,ref}/m_{ref}}$
Cantilever	C1	0.74	0.99	1.82
	C2	0.96	0.96	1.92
Propped cantilever	PC1	0.85	0.85	1.60
	PC2	0.87	0.87	1.60
Simply supported	SS1	0.92	0.91	1.95
	SS2	0.65	0.65	1.38

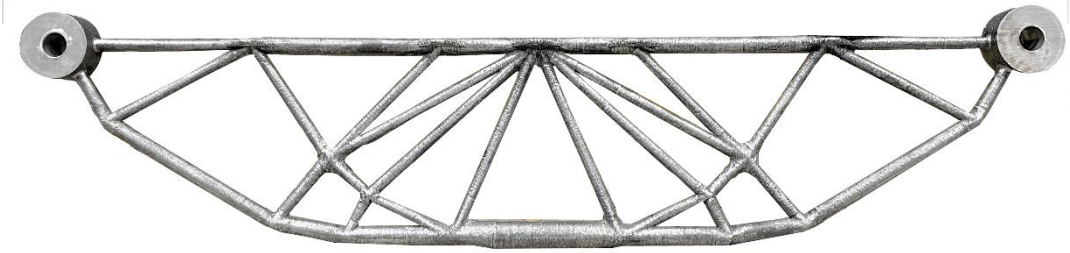
516



(a) Cantilever



(b) Propped cantilever



(c) Simply supported

Figure 1. Optimised trusses: (a) cantilever, (b) propped cantilever and (c) simply supported

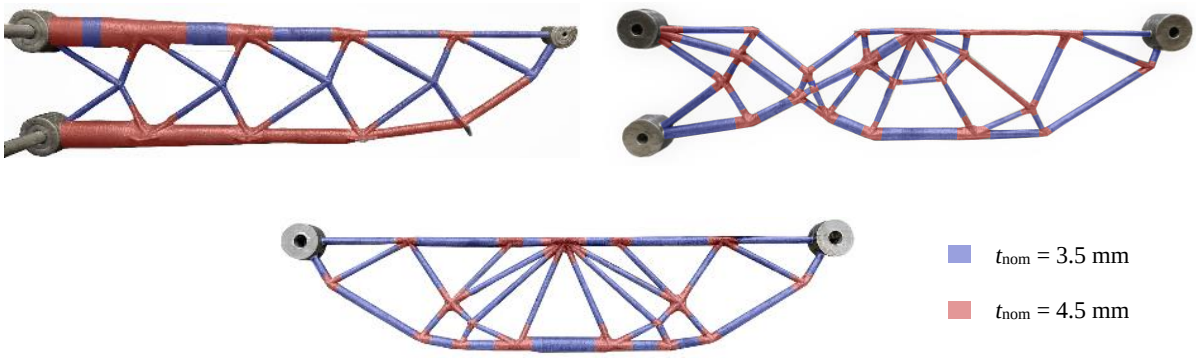
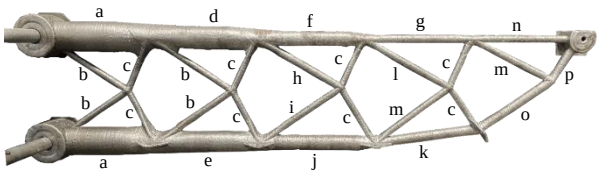
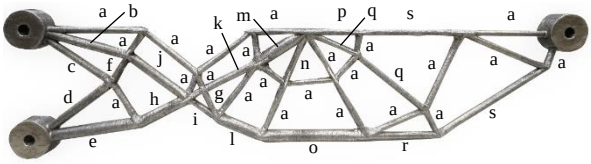


Figure 2. Geometry of optimised trusses, with colour code used to illustrate different nominal thicknesses



a	b	c	d	e	f	j	h
109.8	26.9	25.1	87.3	88.5	57.7	63.3	30.1

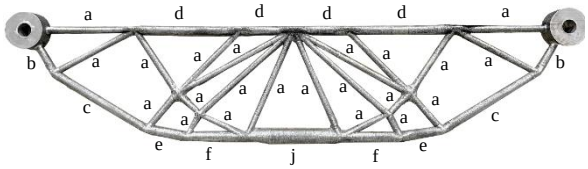
i	g	k	l	m	n	o	p
27.7	33.1	42.7	27.5	26.7	28.1	37.9	32.9



a	b	c	d	e	f
25.1	35.7	27.3	33.1	46.7	25.9

j	h	i	g	k	l
34.1	43.1	25.3	24.9	31.9	44.7

m	n	o	p	q	r	s
50.7	25.7	48.3	27.5	26.5	32.5	29.1



a	b	c	d	e	f	j
25.1	29.9	34.1	34.5	38.5	41.1	60.1

Figure 3. Nominal outer diameters D_{nom} of truss members (in mm)

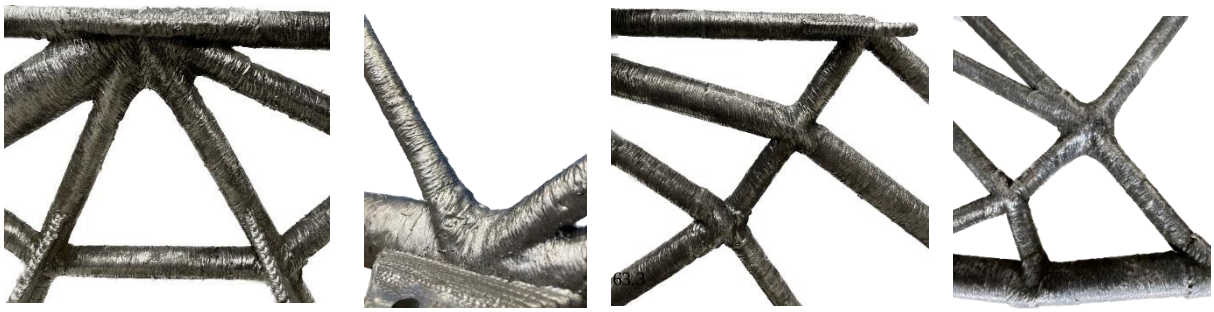
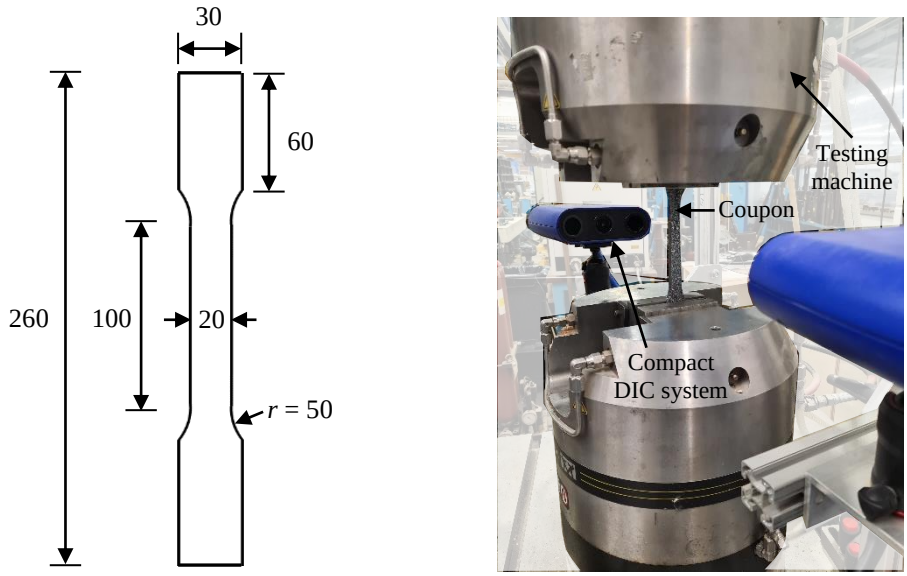
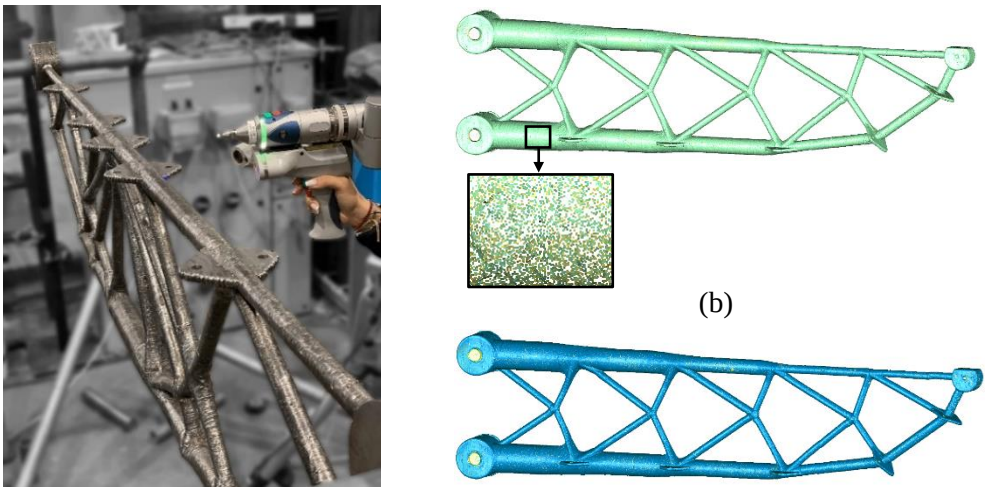


Figure 4. Close-up views of truss nodes



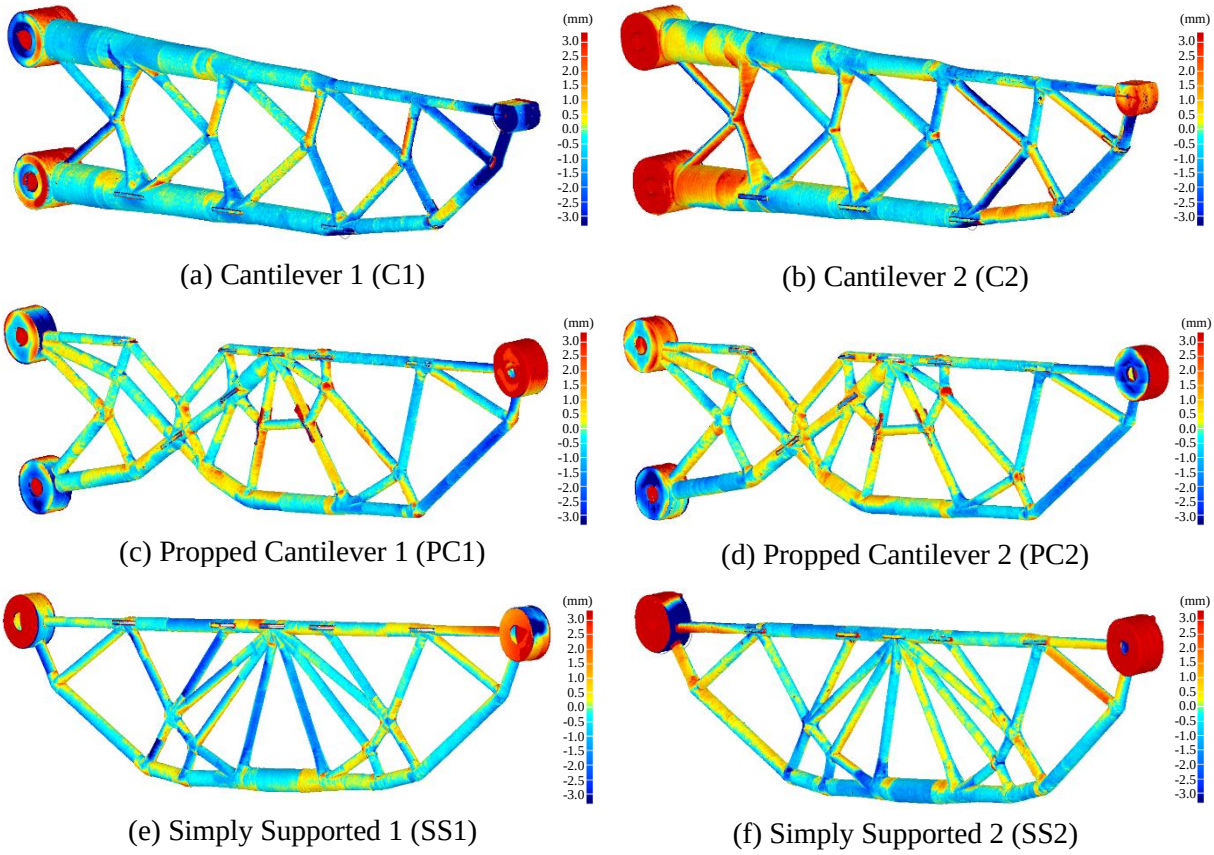
(a) (b)

Figure 5. Tensile coupon tests: (a) coupon dimensions in mm and (b) test setup



(a) (b) (c)

Figure 6. (a) Laser scanning, (b) point cloud and (c) 3D CAD model



(a) Cantilever 1 (C1)

(b) Cantilever 2 (C2)

(c) Propped Cantilever 1 (PC1)

(d) Propped Cantilever 2 (PC2)

(e) Simply Supported 1 (SS1)

(f) Simply Supported 2 (SS2)

Figure 7. Geometric deviation maps of optimised trusses

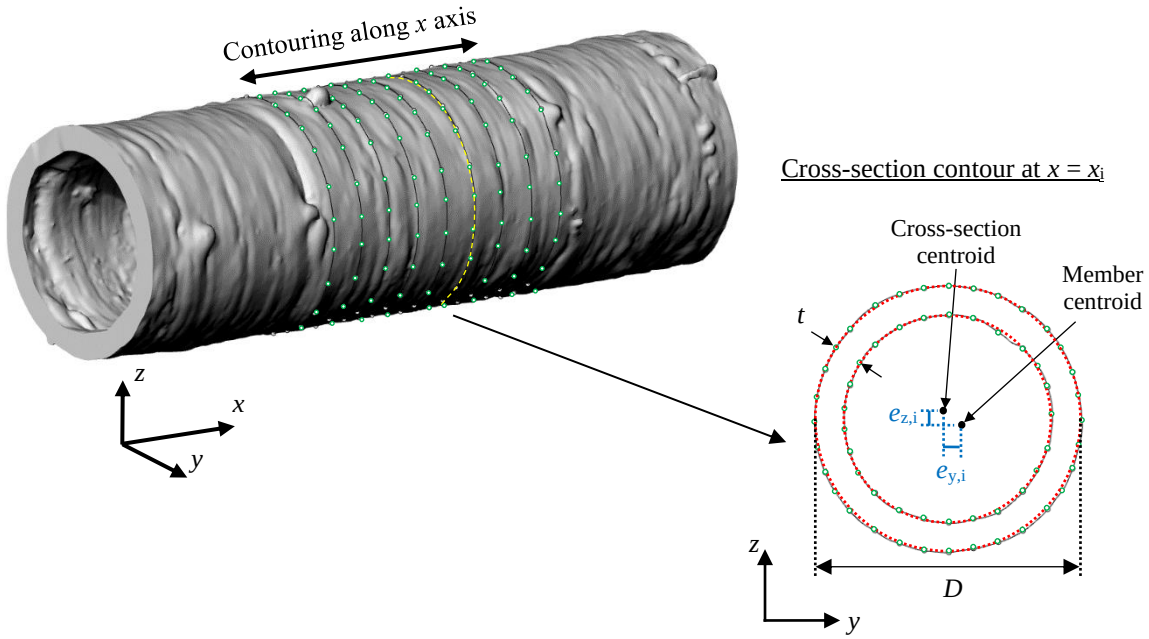


Figure 8. Determination of geometric characteristics of tubular truss members

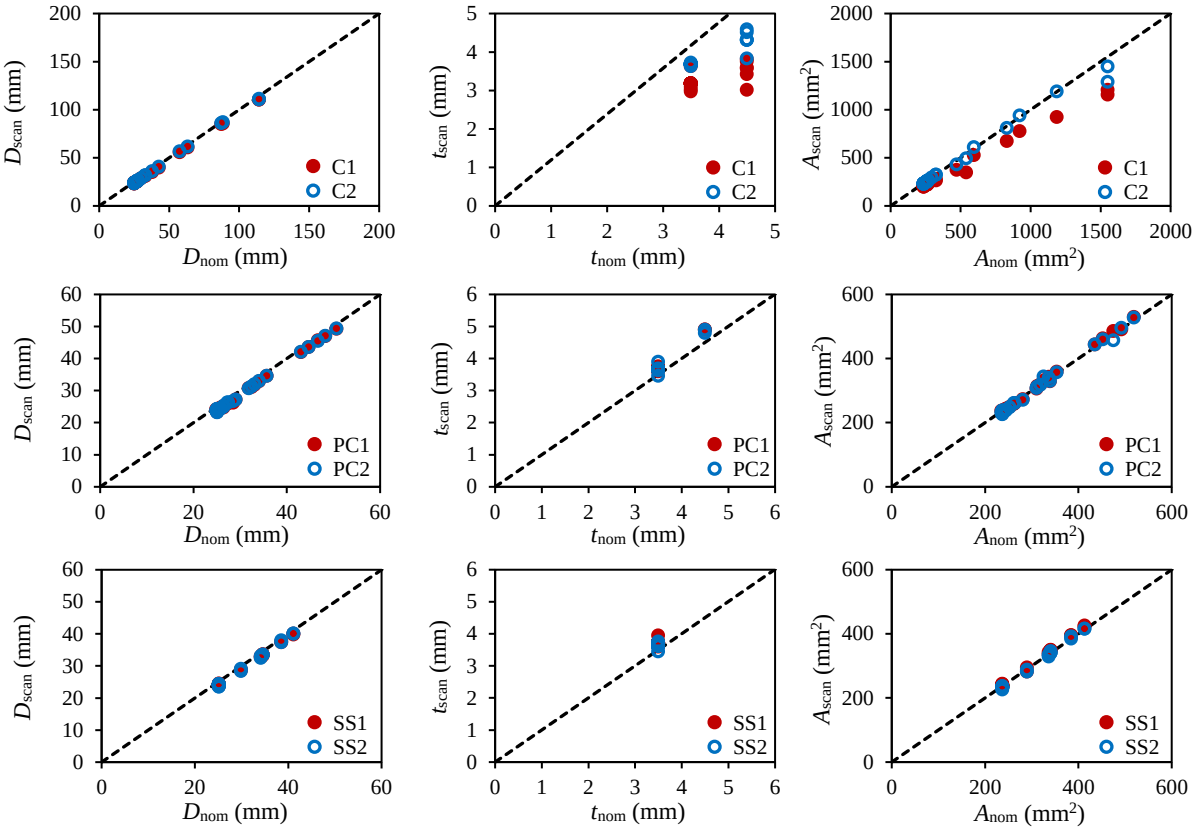


Figure 9. Comparisons between nominal and measured geometric properties of test specimens

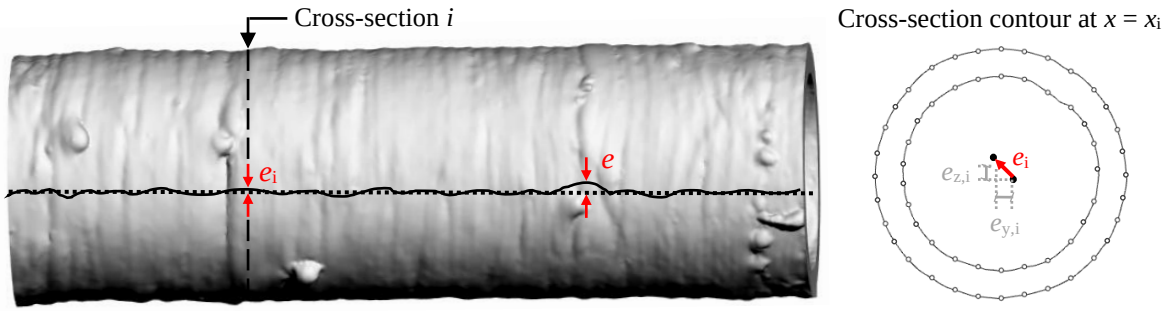


Figure 10. Determination of amplitude of geometric imperfections

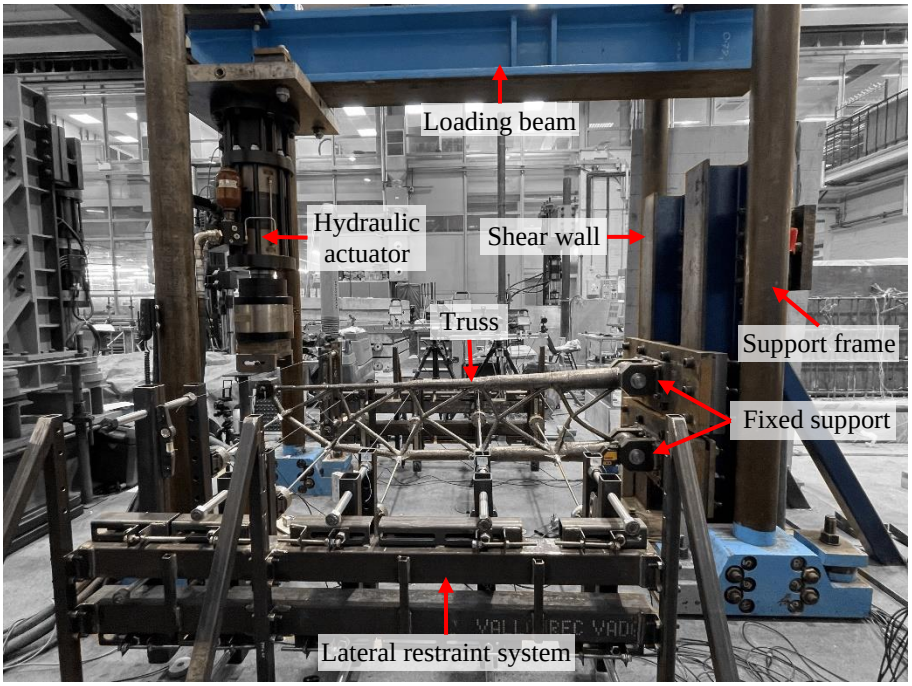


Figure 11. Setup for WAAM optimised truss tests (Specimen C1 shown)



(a) (b) (c) (d)

Figure 12. Configurations for: (a) fixed support, (b) pinned support, (c) roller support and (d) saddle for load application

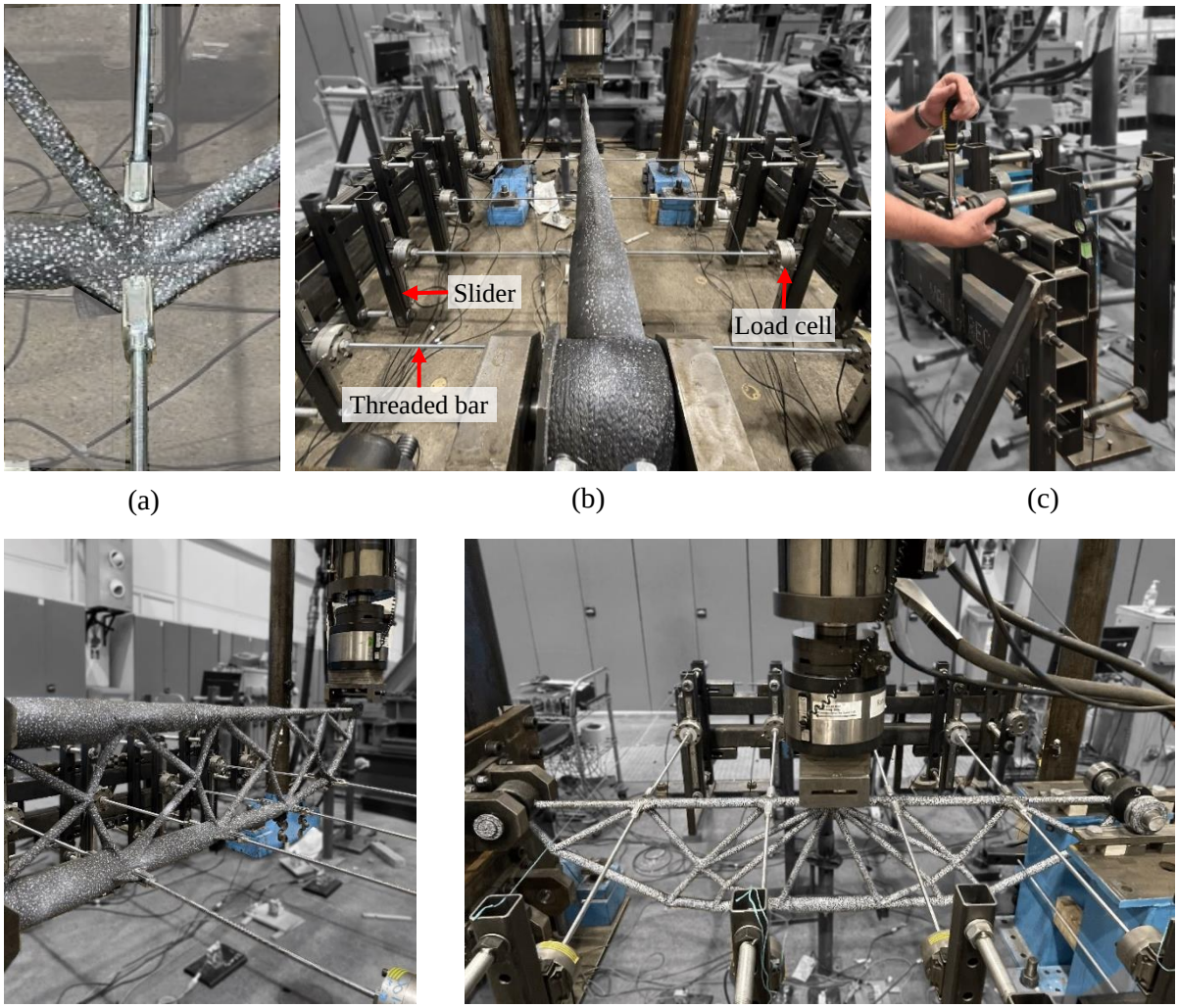


Figure 13. Lateral restraint system: (a) triangular-shaped steel restraints, (b) system components, (c) lateral deflection recovery, (d) cantilever restrained at bottom chord and (e) simply supported truss restrained at top chord

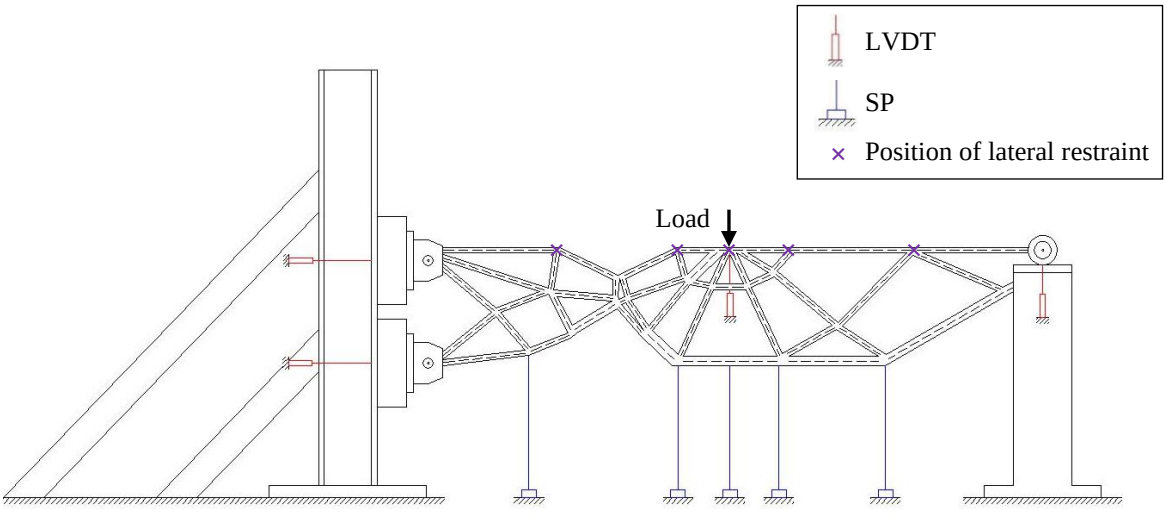


Figure 14. Instrumentation employed in truss tests (shown for propped cantilever)

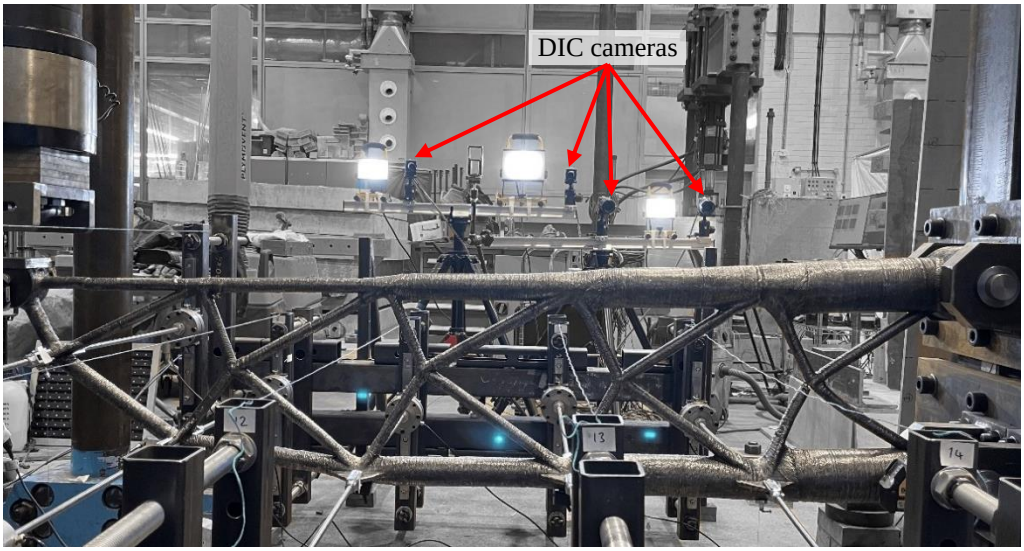


Figure 15. DIC setup employed in truss tests

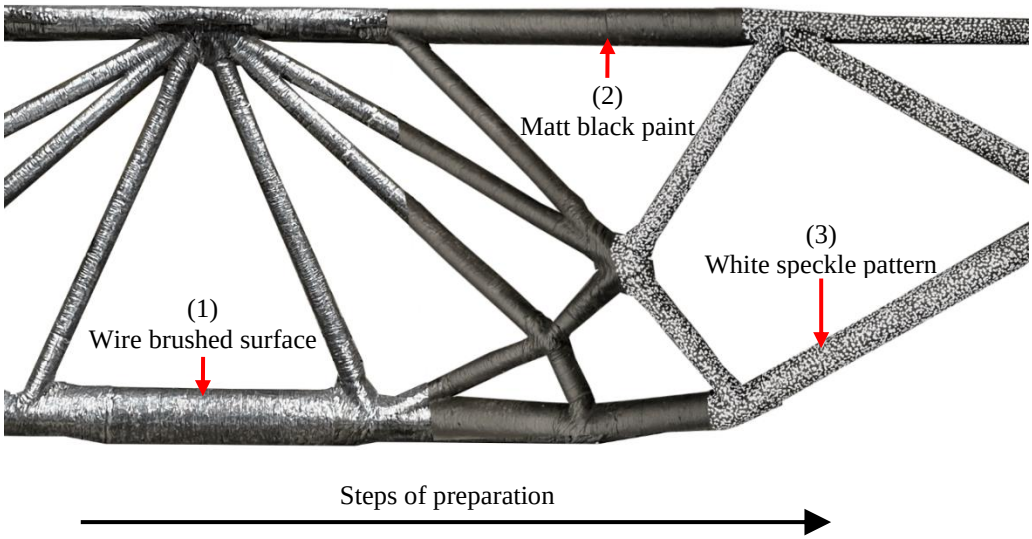
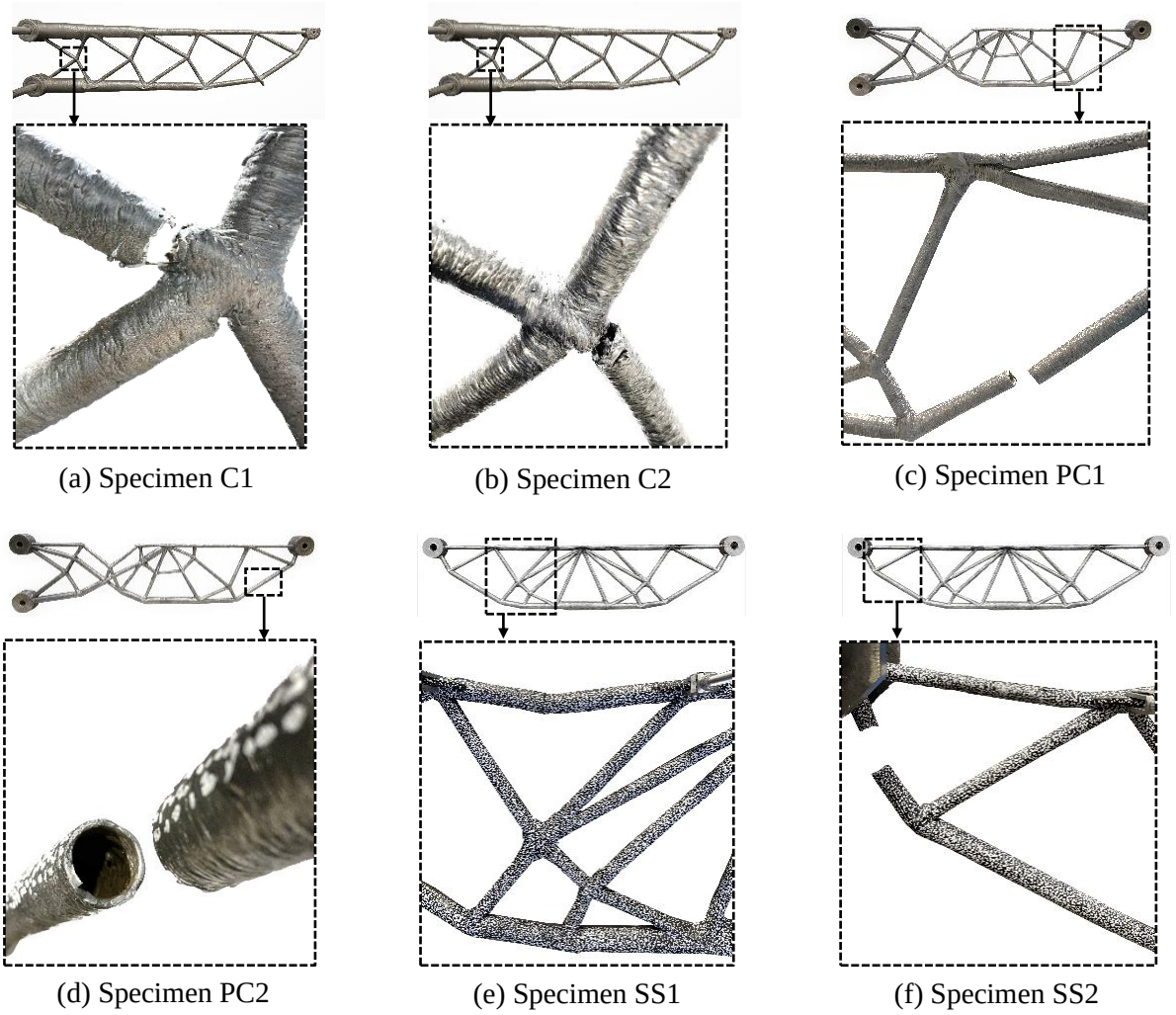


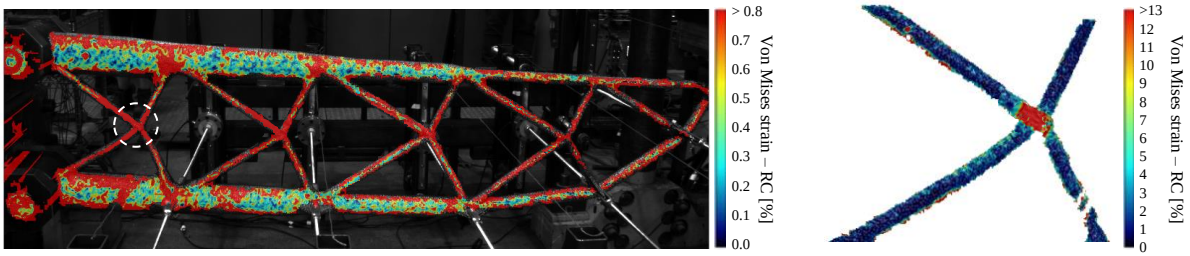
Figure 16. Steps of surface preparation for DIC



(a) Specimen C1 (b) Specimen C2 (c) Specimen PC1

(d) Specimen PC2 (e) Specimen SS1 (f) Specimen SS2

Figure 17. Failure modes of tested specimens, showing: (a) tensile fracture in Specimen C1, (b) tensile fracture in Specimen C2, (c) tensile fracture in Specimen PC1, (d) tensile fracture in Specimen PC2, (e) buckling of top chord member in Specimen SS1 and (f) tensile fracture in Specimen SS2



(a) Overall (b) At fracture location

Figure 18. Typical DIC strain fields at ultimate load: (a) overall and (b) at fracture location

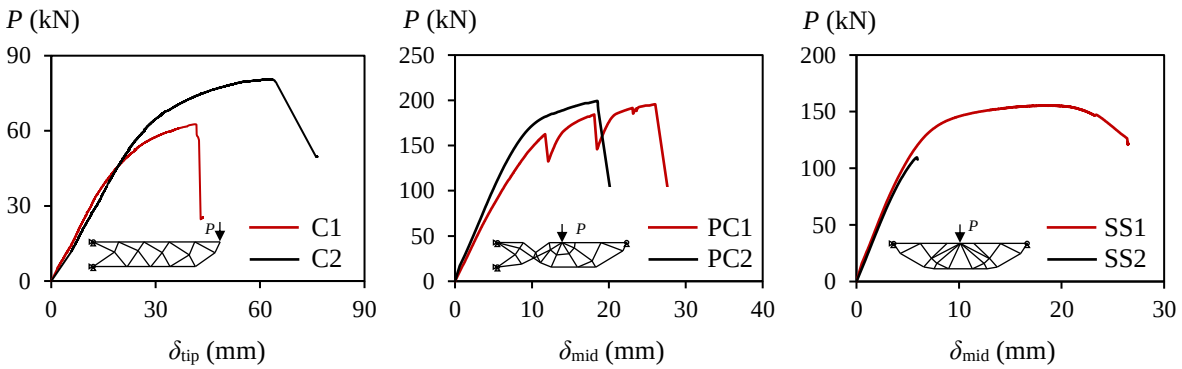
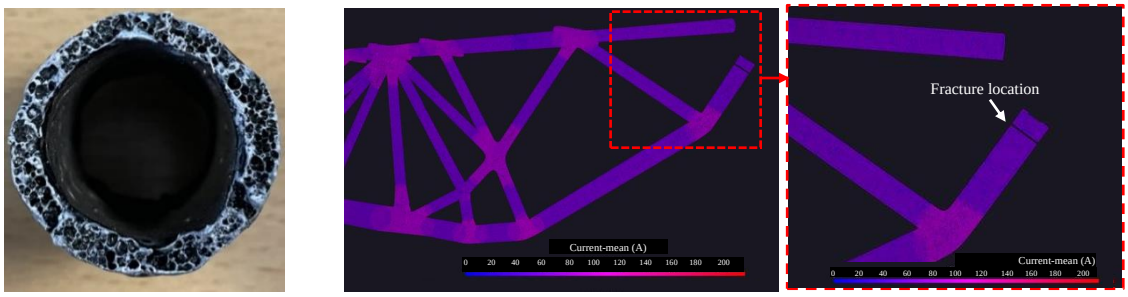
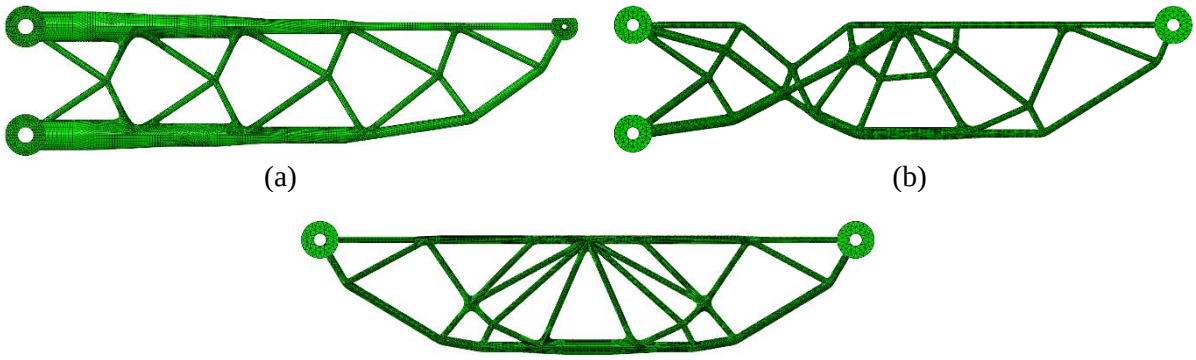


Figure 19. Experimental load-deflection curves for WAAM trusses



(a) (b) (c)

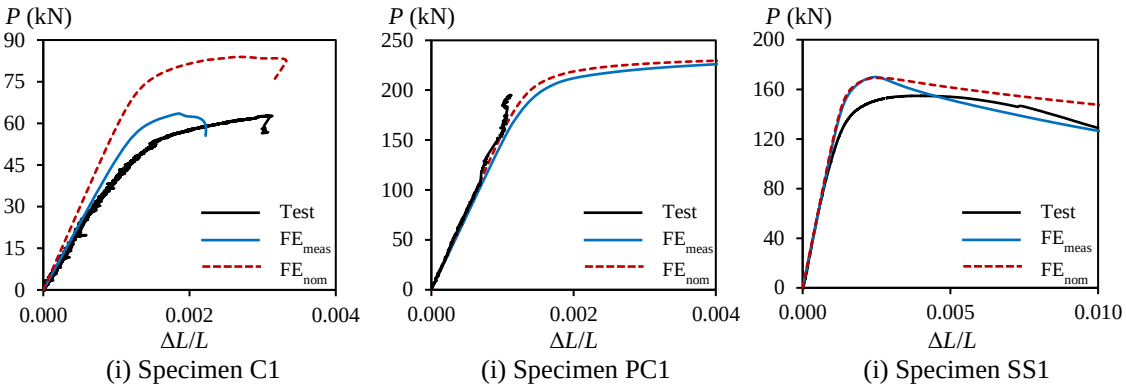
Figure 20. Specimen SS2: (a) porosity at fracture cross-section, (b) log file and (c) close-up view of log file at fracture location

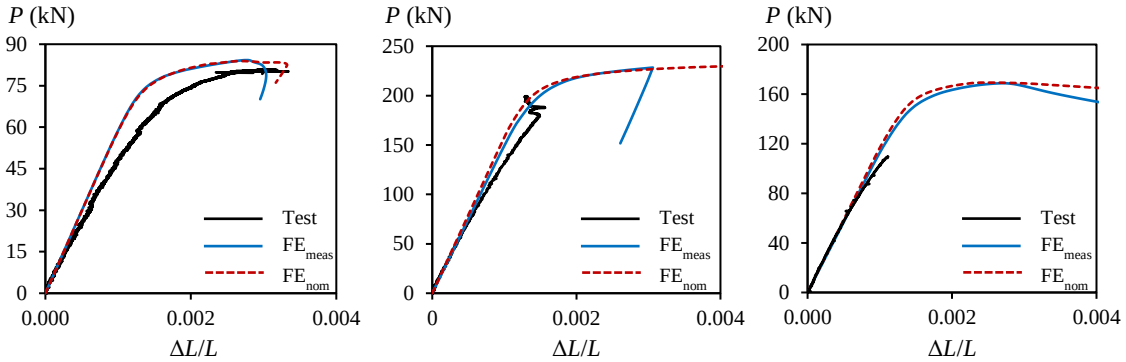


(a) (b)

(c)

Figure 21. FE models of: (a) cantilever, (b) propped cantilever and (c) simply supported trusses





(a) Cantilever trusses (b) Propped cantilever trusses (c) Simply supported trusses

Figure 22. Comparison of test and FE load-deformation curves

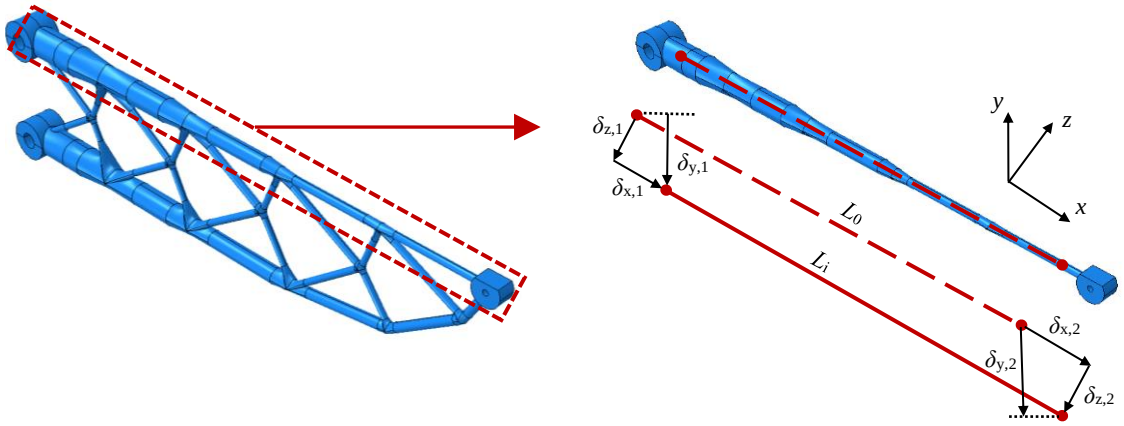


Figure 23. Determination of axial deformation $\Delta L/L$ of top chord

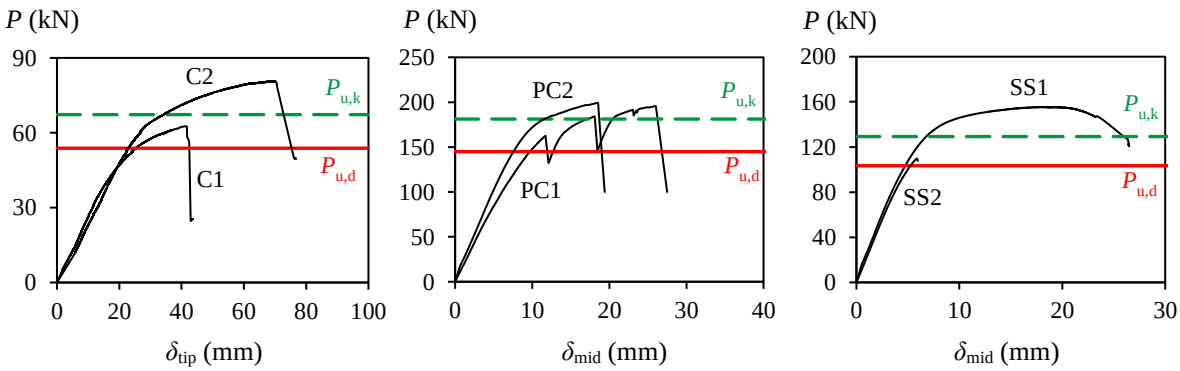


Figure 24. Comparison between test results and design resistances